

Finite time Stückelberg interferometry with nanomechanical modes

Maximilian J. Seitner,^{1,2,*} Hugo Ribeiro,³ Johannes

Kölbl,¹ Thomas Faust,² and Eva M. Weig^{1,2}

¹*Department of Physics, University of Konstanz, 78457 Konstanz, Germany*

²*Center for NanoScience (CeNS) and Fakultät für Physik,
Ludwig-Maximilians-Universität, Geschwister-Scholl-Platz 1, München 80539, Germany*

³*Department of Physics, McGill University,
Montreal, Quebec, H3A 2T8, Canada*

Abstract

Stückelberg interferometry describes the interference of two strongly coupled modes during a double passage through an avoided energy level crossing. In this work, we experimentally investigate finite time effects in Stückelberg interference and provide an exact analytical solution of the Stückelberg problem. Approximating this solution in distinct limits reveals uncharted parameter regimes of Stückelberg interferometry. Experimentally, we study these regimes using a purely classical, strongly coupled nanomechanical two-mode system of high quality factor. The classical two-mode system consists of the in-plane and out-of-plane fundamental flexural mode of a high stress silicon nitride string resonator, coupled via electric gradient fields. The dielectric control and microwave cavity enhanced universal transduction of the nanoelectromechanical system allows for the experimental access to all theoretically predicted Stückelberg parameter regimes. We exploit our experimental and theoretical findings by studying the onset of Stückelberg interference in dependence of the characteristic system control parameters and obtain characteristic excitation oscillations between the two modes even without the explicit need of traversing the avoided crossing. The presented theory is not limited to classical mechanical two-mode systems but can be applied to every strongly coupled (quantum) two-level system, for example a spin-1/2 system or superconducting qubit.

I. INTRODUCTION

Strongly coupled nanomechanical resonators have proven themselves as prominent testbed for the investigation of various fundamental physical concepts. The recent studies of, for example, non-classical correlations^{1,2}, quantum back-action³, quantum squeezing⁴ and topological effects⁵ in different nanomechanical systems demonstrate in an outstanding way the scientific impact of hybrid-mechanical systems. In addition, the high level of control over such coupled resonators allows for the realization of ultrasensitive vectorial force sensors^{6,7} and Λ -type three level systems⁸.

Recently, this high level of control led to the demonstration of classical Stückelberg interference of two strongly coupled nanomechanical resonator modes⁹. This coherent transfer of energy has originally been studied in a broad range of quantum systems including, e.g., spin-1/2 systems^{10–12} and superconducting qubits^{13–17}, amongst many others. Typically, the coherent dynamics of a two-level system in the configuration proposed by Stückelberg¹⁸ is theoretically modeled by an infinite time approach, the so-called adiabatic impulse model¹⁶. Following this model, the interference of two quantum states during a double passage through an avoided level crossing solely relies on the mutual coupling and is independent of the exact time evolution of the two states in the vicinity of the avoided crossing. In this work, we go well beyond this simple approximation and show that the adiabatic impulse model represent just one particular limit, the infinite time limit, of the full Stückelberg problem¹⁸. We provide an exact analytical solution to the problem which captures the importance of finite time effects. By means of asymptotic approximations of the exact finite time solution, we identify up to six different parameter regimes of Stückelberg interferometry. Experimentally, we demonstrate that a classical strongly coupled nanomechanical two-mode system^{9,19} allows for the investigation of all discussed asymptotic regimes due to high mechanical quality factors and hence lifetimes of the coherent mechanical modes in the millisecond regime^{9,19}.

The manuscript is organized as follows. Following this introduction (I), the nanoelectromechanical system as well as the experimental techniques are introduced in the second part (II). In sections III A and III B, we derive an exact analytical solution of the Stückelberg problem, taking advantage of the conformity of classical and quantum interference in this particular problem⁹. Additionally, the asymptotic limits of the exact solution are derived (appendices A & B) which allows for a quantification of characteristic parameter regimes in

Stückelberg interferometry. In chapter III C, we explicitly derive the asymptotic long time limit of the analytical solution. Chapter III D provides a brief summary of previous, approximative theoretical approaches of Stückelberg interferometry and establishes the link to the presented exact analytical solution. Section IV compares the different theories to the experimentally observed classical Stückelberg oscillations of a strongly coupled nanomechanical system. In the last part (V), we summarize the results.

II. THE NANOELECTROMECHANICAL SYSTEM

A. Experimental set-up

We study self-interference of a classical nanomechanical two-mode system using two samples of the same basic design. Sample A is investigated in a pulse-tube cryostat at a temperature of 10 K which serves solely for temperature stabilization. The experiments on sample B are conducted at room temperature. Independent of the ambient temperature, both samples operate deeply in the classical regime and do not exhibit quantum mechanical properties^{9,19}. The samples consist of freely-suspended and doubly clamped silicon nitride (SiN) string resonators, fabricated in a top-down approach from a high-stress silicon nitride film on a fused silica substrate. The 100 nm thick and 270 nm wide silicon nitride strings exhibit a high tensile pre-stress of 1.46 GPa resulting from the LPCVD deposition process of the SiN atop the fused silica wafer. The high tensile pre-stress translates into high mechanical quality factors up to $Q \approx 500,000$ at mechanical resonance frequencies of $\omega_m/2\pi \approx 6.5$ MHz at room temperature. Sample A consists of a 50 μm long string resonator, whereas on sample B we study a 55 μm long string. As depicted in Fig. 1 a and Fig. 1 b, the string resonators exhibit two fundamental flexural vibration modes with orthogonal mode polarizations, namely one perpendicular to the sample plane (out-of-plane) and one parallel to the sample plane (in-plane). For dielectric control and transduction of the string resonators (cf. Fig. 1 c) we process two gold electrodes adjacent to the SiN strings, which form a capacitor and are connected to a microwave cavity²⁰ via a bond wire. The oscillation of the dielectric silicon nitride string between the gold electrodes periodically modulates the capacitance. This change in capacitance in turn modulates the $\lambda/4$ microstrip cavity signal with resonance frequency at approximately $\Omega_c/2\pi \approx 3.6$ GHz by producing sidebands on the

cavity signal at $\Omega_{\pm} = \Omega_c \pm \omega_m$, where $\omega_m/2\pi \approx 6.5$ MHz denotes the mechanical resonance frequency. The modulation induced sidebands are not resolved but can be demodulated via a heterodyne in-phase-quadrature mixing technique²⁰ before subsequent low-pass filtering and amplification. Finally, the demodulated signal is captured using a spectrum analyzer. In addition to the described microwave cavity enhanced heterodyne dielectric detection,

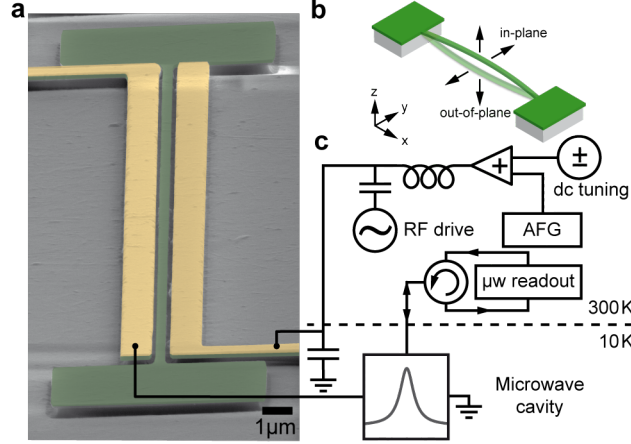


Figure 1. Schematic experimental set-up. **a**, False color scanning electron micrograph of a 50 μm long, 270 nm wide and 100 nm thick silicon nitride string resonator (green) in oblique view. The mechanical resonator is flanked by two 1 μm wide gold electrodes (yellow), which are processed on top of the silicon nitride and form a capacitor providing dielectric drive, tuning and detection as well as mode coupling. **b**, Schematic illustration of the two orthogonally polarized fundamental flexural vibration modes of the silicon nitride string resonator. The oscillation in z -direction, perpendicular to the sample plane, is referred to as out-of-plane oscillation, whereas the oscillation in y -direction, parallel to the sample plane, is referred to as in-plane oscillation. **c**, Schematic equivalent circuit diagram of the electrical drive, tuning and heterodyne detection scheme. The voltage ramp is added to the DC tuning voltage by a summation amplifier and combined with the resonant sinusoidal RF drive tone at a bias tee. The combined voltages are applied to one of the gold electrodes versus the ground of the microwave cavity. The bypass capacitor acts as a ground for the microwave cavity. The microwave cavity is driven on resonance and the signal is read-out via a heterodyne IQ-mixing technique, demodulating the sidebands induced by the oscillation of the nanomechanical resonator.

the gold electrodes are used at the same time for dielectric actuation and control of the mechanical resonance²¹. Applying a DC bias to one of the electrodes induces an electric polarization in the dielectric silicon nitride string, which, in turn, couples to the gradient of the inhomogeneous electric field, generating a gradient force. Adding a resonant sinusoidal RF drive tone with frequency $\omega_m/2\pi$ to the DC voltage at a bias tee results in a periodic force which drives the vibrational resonance of the nanomechanical silicon nitride string resonator²². Approximating the induced electrical polarization by a dipole moment^{21,22}, its magnitude scales linearly with the applied DC voltage. Since the electric field gradient is also directly proportional to the DC voltage, the resonance frequency of the nanomechanical string resonator shifts quadratically with the applied DC bias²¹. By means of careful sample design, the in-plane polarized vibration mode can be engineered to shift downwards in resonance frequency with increasing DC bias, whereas the out-of-plane polarized resonance tunes towards higher resonance frequencies²¹. Thereby, the inherent resonant frequency off-set between the two orthogonally polarized vibration modes, which arises from the rectangular cross-section of the nanomechanical string, can be compensated. Near resonance, the two modes hybridize into normal modes^{6,7,23} of the strongly coupled system, diagonally polarized along $\pm 45^\circ$ with respect to the sample plane. The strong coupling, mediated by the inhomogeneous electric field^{19,23}, is reflected by the pronounced avoided crossing of the two mechanical modes with level splitting $\Delta/2\pi$ as depicted in Fig. 2 a.

B. Measurement scheme

In this work, we study the effects of finite times in classical Stückelberg interferometry. In general, Stückelberg interference¹⁸ occurs during a double passage through an avoided energy level crossing within the coherence time of the strongly coupled system. Both energy branches accumulate phase during the double passage, giving rise to self-interference. This brings about interference fringes depending on the difference in the accumulated phase. The probability to find the system either in the upper or the lower energy branch after the double passage oscillates in dependence of the level splitting, the traversal time as well as the initialization and turning point^{16,18}.

Experimentally, we realize the double passage of the avoided crossing using fast triangular voltage ramps⁹. The voltage ramps are provided by an arbitrary function generator (AFG)

and combined with the fixed DC tuning voltage at a summation amplifier. A detailed description of the ramps can be found in appendix C. In the following, we focus solely on the measurement principle which is equivalent for the investigation of sample A at 10 K and sample B at room temperature. The detailed experimental parameters of the respective samples are discussed in chapter IV. Note that the presented voltage ramp sequence⁹ is analogous to the one employed by Sun *et al.*²⁴ and differs from the frequently performed periodic driving schemes in Stückelberg interferometry experiments¹⁶. The schematic sequence of the applied voltage ramp is depicted in Fig. 2 b. The system is initialized in the lower frequency branch at $\omega_1(U_i)/2\pi$ by the application of a resonant sinusoidal RF drive tone. Hereby, U_i denotes the initialization voltage to which the DC tuning voltage is set during a Stückelberg experiment. Note that this voltage corresponds to a sweep voltage of zero. The sweep voltage defines the additional ramp voltage provided by the AFG. At $t = t_{\text{start}}$, the fast voltage ramp is turned on and detunes the system from the resonant drive at $\omega_1(U_i)/2\pi$. From this time on, the mechanical resonator is not driven any more and its oscillation decays exponentially (green dashed line in Fig. 2 b). Note that the mechanical energy decays on a larger timescale than the duration of the fast voltage ramp. The sweep voltage ramps the system from U_i through the avoided crossing at voltage U_a , up to the absolute peak voltage $\tilde{U}_p = U_i + U_p$ and back to the read-out voltage U_f during time ϑ . At time $t = t_{\vartheta+\varepsilon}$, we start to measure the exponential decay of the mechanical oscillation at frequency $\omega_1(U_f)/2\pi$ in the lower branch at the read-out voltage U_f . The return signal needs to be measured at U_f since the drive at $\omega_1(U_i)/2\pi$ cannot be turned off during the experiment. Hence, a measurement at U_i would lead to another excitation of the mode and therefore destroy the interference. Additionally, the exponential decay of the return signal power needs to be measured with a temporal off-set ε to avoid transient effects. The exponential decay is extrapolated back to the time t_{ϑ} where the voltage ramp ended via a fit and the resulting return signal power is normalized to the signal power at the time of initialization of the resonance ($t = t_{\text{start}}$). This normalization process can lead to return probabilities exceeding a value of unity due to experimental scatter and different characteristic signal power heights at the initialization and read-out voltage. Consequently, we use the term *normalized squared return amplitude* for the experimental data instead of return probability.

For each particular measurement, the voltage ramp has a fixed voltage sweep rate β and fixed peak voltage U_p . The experiment is repeated for a set of different voltage sweep rates

at a fixed peak voltage. Subsequently, the peak voltage is changed and the measurement procedure is repeated. In this way, we investigate classical Stückelberg interferometry as a function of sweep speed and sweep distance which can be absorbed into a single variable, namely time.

In previous approaches¹⁶, Stückelberg interferometry has been investigated in the limit of infinite times. That means the initialization and turning point on the left and the right hand side of the avoided crossing are far away from the point of maximum coupling, which is at voltage U_a where the level splitting is $\Delta/2\pi$, compared to the characteristic time-scale of the system. This infinite time approximation is referred to as the *adiabatic impulse model*¹⁶ and is summarized in chapter III D. In this work, we go beyond this approximation via the investigation of finite time effects. Experimentally, we interface this regime by turning points, i.e. peak voltages, close to or even before the avoided crossing, which still results in characteristic Stückelberg oscillations.

III. FINITE-TIME THEORY

A. Theory of strongly coupled modes

In order to theoretically model the two modes in the strong coupling regime, we follow the work of Novotny *et al.*²⁵ and write the system as two coupled differential equations:

$$\begin{aligned} m\ddot{u}_1(t) + m\omega_1^2 u_1(t) + \kappa [u_1(t) - u_2(t)] &= 0 \\ m\ddot{u}_2(t) + m\omega_2^2 u_2(t) + \kappa [u_2(t) - u_1(t)] &= 0 \end{aligned} \tag{1}$$

where $m = m_0/2$ denotes the effective mass of the resonator with physical mass m_0 , u_j ($j = 1, 2$) the displacement of mode j , $\omega_j = \sqrt{k_j/m}$ the respective angular resonance frequency, k_j the spring constant of mode j , and κ the coupling constant between the two modes. Using the ansatz $u_j(t) = u_{0,j} \exp(-i\omega_\pm t)$ in Eq. (1) yields the resonance frequencies of the two normal modes in the coupled system:

$$\omega_\pm = \frac{\omega_1^2 + \omega_2^2 \pm \sqrt{(\omega_1^2 - \omega_2^2)^2 + 4\Delta^2\omega_1\omega_2}}{2} \tag{2}$$

Here, we define the level splitting

$$\Delta = |\lambda| = \frac{\kappa}{2m\sqrt{\omega_1\omega_2}} = \omega_+ - \omega_-, \tag{3}$$

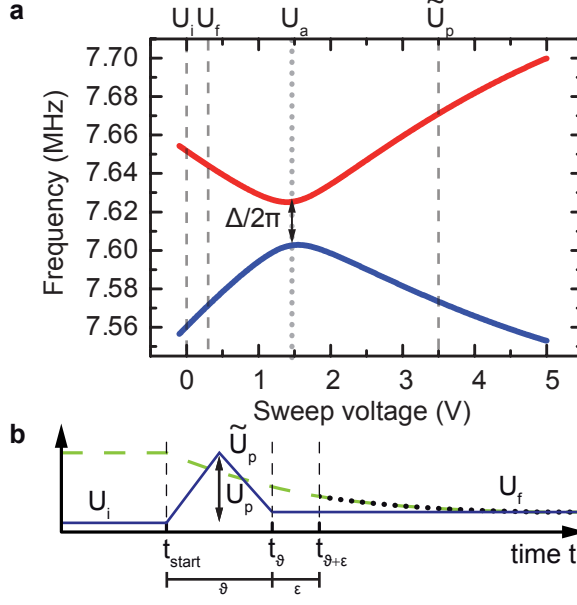


Figure 2. Avoided crossing of sample A and voltage ramp sequence. **a**, Avoided energy level crossing of the two frequency branches (mode 1: blue, mode 2: red) which stem from the two orthogonally polarized flexural modes. Gray dashed lines indicate the initialization voltage U_i , the read-out voltage U_f and an exemplary absolute peak voltage $\tilde{U}_p = U_i + U_p$. The gray dotted line represents the avoided crossing voltage U_a , where the two modes exhibit a frequency splitting of $\Delta/2\pi$. **b**, Temporal evolution of the voltage ramps (blue solid line) defined by the sweep voltage. The ramp starts at $t = t_{\text{start}}$. The sweep voltage is increased from zero to peak voltage U_p at voltage sweep rate β , which increases the absolute voltage from U_i to $\tilde{U}_p = U_i + U_p$. At the apex of the triangular voltage ramp (peak voltage U_p), the sweep voltage is decreased at the same rate to the read-out voltage U_f , which is approached at time $t = t_{\vartheta}$. Hence, the complete triangular voltage ramp has a duration of ϑ . Note that the read-out voltage U_f is off-set from the initialization voltage U_i as explained in the text. As a consequence, the sweep voltage does not return to zero. The ring-down of the mechanical signal power (green dashed line) is measured after a delay ϵ (at time $t = t_{\vartheta} + \epsilon$), and a fit (black dotted line) is used to extract its magnitude at time $t = t_{\vartheta}$. The measured return signal is normalized to the mechanical signal power at $t = t_{\text{start}}$.

where the coupling λ , in general, can be complex valued. If the level splitting exceeds the dissipation in the system, namely the linewidth of the mechanical resonances, the modes can coherently exchange energy on a faster timescale than the energy decay. This strong coupling regime allows for the investigation of time dependent phenomena, like non-adiabatic

Landau-Zener tunneling^{23,25} in the classical regime, coherent dynamics of classical two-mode systems^{19,26,27} and classical state interferometry⁹.

B. Finite-time Stückelberg interferometry

We look for a solution of Eq. (1) in the experimentally relevant limit where $\kappa/k_j \ll 1$, $j \in \{1, 2\}$. This suggests to look for solutions of the form $u_j(t) = c_j(t) \exp[i\tilde{\omega}_1 t]$ with $c_j(t)$ a normalized amplitude, i.e. $|c_1(t)|^2 + |c_2(t)|^2 = 1$, and we define $\tilde{\omega}_j = \sqrt{(k_j + \kappa)/m}$. By replacing our ansatz for $u_j(t)$ in Eq. (1), we find

$$\begin{aligned} \ddot{c}_1(t) + 2i\tilde{\omega}_1 \dot{c}_1(t) - \frac{\kappa}{m} c_2(t) &= 0 \\ \ddot{c}_2(t) + 2i\tilde{\omega}_1 \dot{c}_2(t) + (\tilde{\omega}_2^2 - \tilde{\omega}_1^2) c_2(t) - \frac{\kappa}{m} c_1(t) &= 0, \end{aligned} \quad (4)$$

Since the amplitudes $c_j(t)$ are slowly varying in time compared to the oscillatory function $\exp[i\tilde{\omega}_1 t]$ (see for instance Ref. 28), one can neglect the second derivatives $\ddot{c}_j(t)$ in Eq. (4). Thus, the evolution of the normalized amplitudes is described by

$$i\dot{\mathbf{c}}(t) = H(t)\mathbf{c}(t), \quad (5)$$

where we have defined $\mathbf{c}(t) = (c_1(t) \ c_2(t))^T$ and

$$H(t) = \begin{pmatrix} 0 & \frac{\lambda}{2} \\ \frac{\lambda}{2} & -\alpha t \end{pmatrix}, \quad (6)$$

with $\lambda = \kappa/(m\tilde{\omega}_1)$. To obtain Eq. (6), we have used that in the vicinity of the avoided crossing $\tilde{\omega}_2 \simeq \tilde{\omega}_1$. This yields $(\tilde{\omega}_2^2 - \tilde{\omega}_1^2)/(2\tilde{\omega}_1) \simeq \tilde{\omega}_2 - \tilde{\omega}_1$ and we assume that the difference in frequency is changed in time such that $\tilde{\omega}_2 - \tilde{\omega}_1 \simeq \alpha t$, where α denotes the frequency sweep rate. Note that we employ the frequency sweep rate α in the theory which is converted to the experimentally accessible voltage sweep rate β using the conversion factor ζ from frequency to voltage (cf. section IV A and Ref. 9):

$$\alpha = 2\pi \times \zeta \times \beta. \quad (7)$$

By applying the time-dependent unitary transformation

$$S(t) = \exp\left[i\frac{\alpha}{4}t^2\right] \mathbb{1}_2, \quad (8)$$

to Eq. (5), with $\mathbb{1}_2$ the two-dimensional identity operator, we find that the transformed amplitudes obey the differential equation

$$i\dot{\mathbf{c}}_{\text{LZ}}(t) = H_{\text{LZ}}(t)\mathbf{c}_{\text{LZ}}(t) \quad (9)$$

where the dynamical matrix

$$H_{\text{LZ}}(t) = \frac{1}{2} \begin{pmatrix} \alpha t & \lambda \\ \lambda & -\alpha t \end{pmatrix} \quad (10)$$

is analog to the representation of the Landau-Zener Hamiltonian in the basis of diabatic states. Thus, the finite-time solution of the Landau-Zener problem²⁹ is also a solution of Eq. (9). By analogy with the quantum mechanical case, we express the solution using a classical flow φ_{LZ} (see for instance Hamiltonian flow in Ref. 30),

$$\mathbf{c}_{\text{LZ}}(t) = \varphi_{\text{LZ}}(t, t_i)\mathbf{c}_{\text{LZ}}(t_i), \quad (11)$$

with $\mathbf{c}_{\text{LZ}}(t_i)$ the initial condition of the system and

$$\varphi_{\text{LZ}}(t, t_i) = \begin{pmatrix} \varphi_{\text{LZ},11}(t, t_i) & \varphi_{\text{LZ},12}(t, t_i) \\ -\varphi_{\text{LZ},12}^*(t, t_i) & \varphi_{\text{LZ},11}^*(t, t_i) \end{pmatrix}. \quad (12)$$

We have

$$\varphi_{\text{LZ},11}(t, t_i) = \frac{\Gamma\left(1 + i\frac{\eta^2}{4}\right)}{\sqrt{2\pi}} \left[D_{-1-i\frac{\eta^2}{4}} \left(e^{-i\frac{3\pi}{4}} \tau_i \right) D_{-i\frac{\eta^2}{4}} \left(e^{i\frac{\pi}{4}} \tau \right) + D_{-1-i\frac{\eta^2}{4}} \left(e^{i\frac{\pi}{4}} \tau_i \right) D_{-i\frac{\eta^2}{4}} \left(e^{-i\frac{3\pi}{4}} \tau \right) \right] \quad (13)$$

and

$$\varphi_{\text{LZ},12}(t, t_i) = \frac{\Gamma\left(1 + i\frac{\eta^2}{4}\right)}{\sqrt{2\pi}} \frac{2}{\eta} e^{-i\frac{\pi}{4}} \left[D_{-i\frac{\eta^2}{4}} \left(e^{-i\frac{3\pi}{4}} \tau_i \right) D_{-i\frac{\eta^2}{4}} \left(e^{i\frac{\pi}{4}} \tau \right) - D_{-i\frac{\eta^2}{4}} \left(e^{i\frac{\pi}{4}} \tau_i \right) D_{-i\frac{\eta^2}{4}} \left(e^{-i\frac{3\pi}{4}} \tau \right) \right], \quad (14)$$

where we have introduced dimensionless quantities by defining $\tau = \sqrt{\alpha}t$ and $\eta = \lambda/\sqrt{\alpha}$.

Finally, the flow describing the evolution of $c_1(t)$ and $c_2(t)$ is given by

$$\varphi(t, t_i) = \exp \left[\frac{i}{4} (\tau^2 - \tau_i^2) \right] \varphi_{\text{LZ}}(t, t_i). \quad (15)$$

The flow $\varphi(t, t_i)$ allows us to write in a simple way the state of the system after multiple passages through the avoided crossing. In particular, for a double passage we have

$$\mathbf{c}(t) = \varphi_{\text{b}}(t, -t_{\text{p}})\varphi(t_{\text{p}}, t_i)\mathbf{c}(t_i), \quad (16)$$

with $\varphi_b(t, t_i) = \sigma_x \varphi(t, t_i) \sigma_x$ describing the evolution of the system during the back sweep, σ_x denotes the Pauli matrix in x -direction, and t_p labels the time at which the forward (backward) sweep stops (starts). The fact that $\varphi_b(t, t_i) = \sigma_x \varphi(t, t_i) \sigma_x$ can be understood by noticing that during the back sweep the frequency of mode 1 (2) decreases (increases) while it increases (decreases) during the forward sweep (see Fig. 2 a).

From Eq. (16), one obtains the return probability to mode 1,

$$P_{1 \rightarrow 1} = |\varphi_{11}(t_p, t_i) \varphi_{11}^*(t, -t_p) + \varphi_{12}^*(t_p, t_i) \varphi_{12}^*(t, -t_p)|^2. \quad (17)$$

C. Asymptotic solution for the long-time limit

1. Long time limit

In this section, we show how to obtain an approximate form of Eq. (17) in the long-time limit, i.e. $\tau, |\tau_i|, \tau_p \gg 1$. Using the respective asymptotic expansion of the parabolic cylinder function (see appendix A), we find

$$\begin{aligned} \varphi_{LZ,11}(t, t_i) \simeq & \sqrt{1 - e^{-\pi \frac{\eta^2}{2}}} \left[\sin[\theta(|\tau_i|)] \cos[\theta(\tau)] e^{i \left(\xi(|\tau_i|) + \xi(\tau) + \frac{\pi}{4} - \arg \left[\Gamma \left(1 + i \frac{\eta^2}{4} \right) \right] \right)} \right. \\ & \left. + \cos[\theta(|\tau_i|)] \sin[\theta(\tau)] e^{-i \left(\xi(|\tau_i|) + \xi(\tau) + \frac{\pi}{4} - \arg \left[\Gamma \left(1 + i \frac{\eta^2}{4} \right) \right] \right)} \right] \\ & + e^{-\pi \frac{\eta^2}{4}} \left[\cos[\theta(|\tau_i|)] \cos[\theta(\tau)] e^{i[\xi(|\tau_i|) - \xi(\tau)]} - \sin[\theta(|\tau_i|)] \sin[\theta(\tau)] e^{-i[\xi(|\tau_i|) - \xi(\tau)]} \right] \end{aligned} \quad (18)$$

and

$$\begin{aligned} \varphi_{LZ,12}(t, t_i) \simeq & \sqrt{1 - e^{-\pi \frac{\eta^2}{2}}} \left[-\sin[\theta(|\tau_i|)] \sin[\theta(\tau)] e^{i \left(\xi(|\tau_i|) + \xi(\tau) + \frac{\pi}{4} - \arg \left[\Gamma \left(1 + i \frac{\eta^2}{4} \right) \right] \right)} \right. \\ & \left. + \cos[\theta(|\tau_i|)] \cos[\theta(\tau)] e^{-i \left(\xi(|\tau_i|) + \xi(\tau) + \frac{\pi}{4} - \arg \left[\Gamma \left(1 + i \frac{\eta^2}{4} \right) \right] \right)} \right] \\ & + e^{-\pi \frac{\eta^2}{4}} \left[\cos[\theta(|\tau_i|)] \sin[\theta(\tau)] e^{-i[\xi(|\tau_i|) - \xi(\tau)]} - \sin[\theta(|\tau_i|)] \cos[\theta(\tau)] e^{i[\xi(|\tau_i|) - \xi(\tau)]} \right]. \end{aligned} \quad (19)$$

The functions $\cos[\theta(\tau)]$, $\sin[\theta(\tau)]$, and $\xi(\tau)$ are defined in appendix A and $\Gamma(z)$ is the gamma function.

Substituting these expressions in Eq. (17) yields an expression for the return probability that is valid in the long time limit. Note that the expansions in Eq. (18) and Eq. (19) are also valid for the softer criteria $\tau^2 + \eta^2/4 > 1$, $\tau_i^2 + \eta^2/4 > 1$, and $\tau_p^2 + \eta^2/4 > 1$.

2. Infinite time limit

If one further assumes that $\eta/\tau, \eta/|\tau_i|, \eta/\tau_p \ll 1$, then $\cos[\theta(\tau)]$ and $\sin[\theta(\tau)]$ can be expanded in powers of η/τ . We find $\cos[\theta(\tau)] = 1 + \mathcal{O}(\eta^2/\tau^2)$ and $\sin[\theta(\tau)] = \mathcal{O}(\eta/\tau)$. In this limit, which we refer to as the infinite-time limit, the return probability becomes

$$P_{1 \rightarrow 1}^{\text{inf}} = 1 - 4P_{\text{LZ}}(1 - P_{\text{LZ}})\cos^2[\chi_{\text{dp}}(\tau_p)] + \mathcal{O}\left(\frac{\eta}{\tau}, \frac{\eta}{\tau_i}, \frac{\eta}{\tau_p}\right), \quad (20)$$

where $P_{\text{LZ}} = \lim_{t_i \rightarrow -\infty, t \rightarrow \infty} |\varphi_{11}(t, t_i)|^2 = \exp(-\pi\eta^2/2)$ is the Landau-Zener(-Stückelberg-Majorana) non-adiabatic transition probability^{18,31–33} and we have defined the phase acquired during the double passage

$$\chi_{\text{dp}}(\tau) = -\frac{\eta^2}{4} + \frac{\eta^2}{2} \log \left[\frac{1}{2} \left(\tau + \sqrt{\tau^2 + \eta^2} \right) \right] + \frac{\tau}{2} \sqrt{\tau^2 + \eta^2} - \arg \left[\Gamma \left(1 + i\frac{\eta^2}{4} \right) \right] - \frac{\pi}{4}. \quad (21)$$

As we will show below, Eq. (20) can also be found using the so-called *adiabatic impulse model*. While the latter model allows one to easily find an expression of the return probability in the limit $\eta/\tau, \eta/|\tau_i|, \eta/\tau_p \ll 1$, it is very hard to extend the adiabatic impulse model to other parameter regimes. Another drawback of the adiabatic impulse model is that the leading order corrections to Eq. (20) cannot be found. In appendix B, we give an expression for the leading order correction to Eq. (20), which demonstrates that even in the infinite-time limit the return probability depends explicitly on τ_i and τ .

D. Adiabatic impulse model

In this section, we briefly recapitulate a previous theoretical approach to Stückelberg interferometry known as the *adiabatic impulse model*¹⁶. The main assumptions of the adiabatic impulse model are that all non-adiabatic transitions happen at $\tau = 0$ and that the system follows perfect adiabatic evolution from $\tau_i \rightarrow 0_-$ and from $0_+ \rightarrow \tau_p$, where $|\tau_i| \gg \eta$ with $\tau_i < 0$ and $\tau_p \gg \eta$. Given the assumptions of the model, it is convenient to work in the basis of instantaneous eigenstates of Eq. (10).

The non-adiabatic part of the evolution is described with a scattering matrix that relates the probability amplitudes right before the avoided crossing at $t = 0_-$ and right after the avoided crossing at $t = 0_+$. The scattering matrix (in the basis of instantaneous eigenstates)

reads¹⁶

$$N = \begin{pmatrix} \sqrt{1 - P_{\text{LZ}}} e^{-i(\chi_s - \frac{\pi}{2})} & -\sqrt{P_{\text{LZ}}} \\ \sqrt{P_{\text{LZ}}} & \sqrt{1 - P_{\text{LZ}}} e^{i(\chi_s - \frac{\pi}{2})} \end{pmatrix}. \quad (22)$$

Here, $\chi_s = \pi/4 + (\eta^2/4)[\log(\eta^2/4) - 1] - \arg[\Gamma(1 + i\eta^2/4)]$ is the so-called Stokes phase³⁴.

The adiabatic part of the evolution is described by the unitary evolution operator

$$U_{\text{ad}}(\tau, \tau_i) = \exp[-i\chi_{\text{dyn}}(\tau, \tau_i)\sigma_z], \quad (23)$$

with σ_z the Pauli matrix in the z-direction and we have defined the dynamical phase

$$\begin{aligned} \chi_{\text{dyn}}(\tau, \tau_i) &= \frac{1}{2} \int_{\tau_i}^{\tau} d\tau_1 \sqrt{\tau_1^2 + \eta^2} \\ &= \frac{1}{4} \left(\tau \sqrt{\tau^2 + \eta^2} + \eta^2 \log \left[\tau + \sqrt{\tau^2 + \eta^2} \right] - \tau_i \sqrt{\tau_i^2 + \eta^2} - \eta^2 \log \left[\tau_i + \sqrt{\tau_i^2 + \eta^2} \right] \right). \end{aligned} \quad (24)$$

Within this formalism, the state of the system after a double passage is given by

$$\mathbf{c}_{\text{LZ}}(\tau) \simeq U_{\text{ad}}(\tau, -0_-) N U_{\text{ad}}(-0_+, -\tau_p) U_{\text{ad}}(\tau_p, 0_+) N U_{\text{ad}}(0_-, -|\tau_i|) \mathbf{c}_{\text{LZ}}(-|\tau_i|). \quad (25)$$

Here, we have chosen 0_- and 0_+ to represent fixed times along the time axis. Note that we employ the scattering matrix N instead of its Hermitian conjugate in the back sweep. Since the scattering matrix is expressed in the basis of instantaneous eigenstates, there is no difference in which direction the non-adiabatic transition is performed.

In general, all four adiabatic evolution operators in Eq. (25) contribute to the acquired dynamical phase of the system. For the particular case of the presented experiment, we initialize the system in an eigenstate of the coupled system, which is the out-of-plane mode. In this scenario, the first and the last adiabatic evolution operators in Eq. (25) turn into global phases, which do not contribute to the two-mode interference. Hence, the interference of the two modes is solely governed by the phase evolution in between the two scattering matrices. Finally, the adiabatic impulse model yields the return probability

$$P_{1 \rightarrow 1}^{\text{aip}} = 1 - 4P_{\text{LZ}}(1 - P_{\text{LZ}}) \cos^2[\chi_{\text{dp}}(\tau)], \quad (26)$$

where we have used the fact that in the infinite-time limit ($\eta/\tau \ll 1$) the instantaneous eigenstates and diabatic states of Eq. (10) coincide with each other.

As mentioned earlier, we have $P_{1 \rightarrow 1}^{\text{aip}} = P_{1 \rightarrow 1}^{\text{inf}}$. The main difficulty in using the adiabatic impulse model to get the return probability in regimes other than $\eta/\tau \ll 1$ lies in finding an appropriate scattering matrix N that explicitly depends on time.

IV. COMPARISON OF EXPERIMENT AND THEORIES

A. Stückelberg oscillations

In this chapter, we compare the experimental results, taken with two different samples, with the theoretical models from chapter III. The measurements on sample A are performed at a temperature of 10 K in a pulse tube cryostat. The 50 μm long nanomechanical string resonator exhibits a linewidth of the mechanical resonance $\Gamma/2\pi \approx 40$ Hz at the out-of-plane resonance frequency $\omega_1(U_i)/2\pi = 7.560$ MHz and hence a quality factor $Q = \omega_1/\Gamma \approx 2 \times 10^5$. Here, $U_i = 7.9$ V is the initialization voltage. The two strongly coupled mechanical modes exhibit a frequency splitting of $\Delta/2\pi = 22.614$ kHz at the avoided crossing voltage $U_a = U_i + 1.471$ V = 9.731 V. The conversion factor from frequency sweep rate α to voltage sweep rate β is determined from the avoided crossing via a linear fit⁹ as $\zeta = 55.042$ kHz/V. Figure 3 depicts the measured normalized squared return amplitude versus inverse voltage sweep rate $1/\beta$ for a fixed peak voltage $U_p = 2.5$ V and read-out voltage $U_f = U_i + 0.2$ V = 8.1 V. The experimentally taken data (blue points) is compared to the different theoretical predictions calculated from the above parameters. The red solid line represents the exact solution following Eq. (17), whereas the green dashed line depicts the asymptotic theory (see appendix A) and the black dotted line shows the results from the adiabatic impulse model [Eq. (26)]. We find the experimental data in good agreement with the exact solution via finite times and the asymptotic theory, where the latter nearly coincides with the exact finite time solution. Explicitly, the accumulation of phase and hence the state interference is determined by the exact evolution of the two frequency branches in time in combination with the coupling of the modes. This dependence can be absorbed in characteristic times and an effective coupling η , determined by the sweep rate and the voltages of initialization, avoided crossing, turning-point and read-out:

$$\begin{aligned}
 t_i &= -\frac{1}{\beta}(U_a - U_i) = \frac{\tau_i}{\sqrt{\alpha}} \\
 t_p &= \frac{1}{\beta}(\tilde{U}_p - U_a) = \frac{\tau_p}{\sqrt{\alpha}} \\
 t_f &= \frac{1}{\beta}(U_a - U_f) = \frac{\tau_f}{\sqrt{\alpha}} \\
 \eta &= \frac{\Delta}{\sqrt{2\pi\zeta\beta}} = \frac{\Delta}{\sqrt{\alpha}}.
 \end{aligned} \tag{27}$$

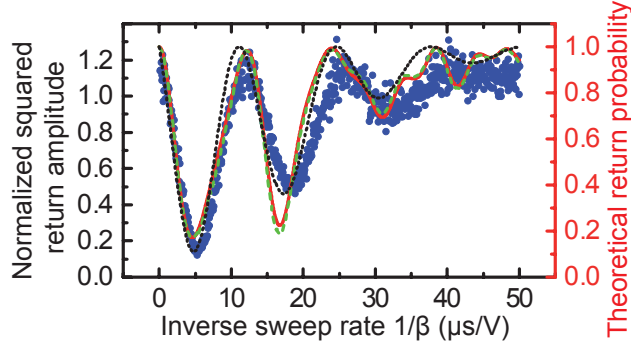


Figure 3. Classical Stückelberg interferometry measured on sample A. Normalized squared return amplitude versus inverse sweep rate $1/\beta$ for a peak voltage of $U_p = 2.5$ V measured on sample A (left axis, blue dots). Right axis (red): Comparison of the different theoretical models calculated with a single set of parameters extracted from the experimental data; exact solution via finite times (red solid line), asymptotic theory (green dashed line) and adiabatic impulse model (black dotted line).

Note that in the definition of t_p , the absolute peak voltage \tilde{U}_p appears instead of the peak voltage of the applied voltage ramp U_p (see Fig. 2 b).

The Stückelberg return probability predicted by the adiabatic impulse model exhibits good agreement with the experimental data as well. Nevertheless, distinct features appearing in the exact finite time solution and the asymptotic theory are not reproduced by the adiabatic impulse model. This can be understood as follows: From the experimental parameters in Fig. 3 we find the system to operate in the limit of *infinite times* (cf. chapter III C 2) since $\eta/\tau_f \approx 0.05, \eta/|\tau_i| \approx 0.04, \eta/\tau_p \approx 0.06 \ll 1$. As detailed in appendix B, the adiabatic impulse model corresponds to the zeroth order series expansion of $\cos[\theta(\tau)]$ and $\sin[\theta(\tau)]$ in the long time limit of the asymptotic solution. Taking into account higher order corrections to the return probability would result in the appearance of the distinct features of the exact solution in the extended adiabatic impulse model.

In order to investigate the validity of the different theoretical approaches, we perform Stückelberg interferometry experiments for a large set of peak voltages U_p at room temperature using a second sample. In particular, we study the finite time dynamics of the system for absolute peak voltages, i.e. turning points, close to the avoided crossing and even observe interference without traversing the latter. The sample measured at room temperature

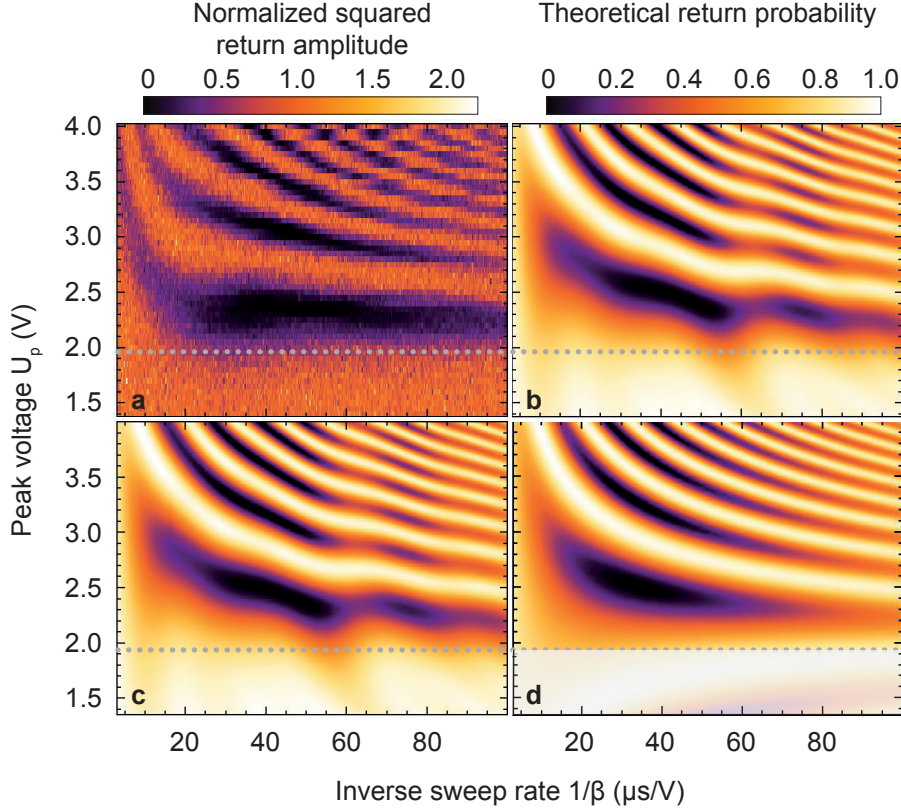


Figure 4. Comparison of experiment and different theoretical models on Stückelberg interferometry measured on sample B. **a**, Color-coded (left colorbar) normalized squared return amplitude versus peak voltage U_p and inverse sweep rate $1/\beta$. Gray dotted line indicates the position of the avoided crossing at voltage $U_p = 1.958$ V in all sub-panels. **b-d**, Color-coded theoretical return probability (right colorbar) calculated from a single set of parameters, extracted from the experimental data, for the exact finite time solution (**b**), the asymptotic theory (**c**) and the adiabatic impulse model (**d**). The mechanical damping is modelled according to Eq. (28) in all theory plots (**b-d**). Note that the adiabatic impulse model (**d**) is plotted for the same parameter range without respect to the physical validity in certain ranges. The region for peak voltages $\tilde{U}_p < U_{B,a}$ is manually grayed out as explained in the text.

(sample B, denoted "B") incorporates the same basic design as sample A except the length of the nanomechanical string resonator of $55 \mu\text{m}$. However, sample B exhibits a mechanical resonance linewidth of $\Gamma_B/2\pi \approx 25$ Hz at frequency $\omega_{B,1}(U_{B,i})/2\pi = 6.561$ MHz and consequently provides an enhanced mechanical lifetime of 6.21 ms. The system is initialized at $U_{B,i} = 10.4$ V, again in the lower frequency branch, and read-out at $U_{B,f} = U_{B,i} + 0.5$ V =

10.9 V. The two modes exhibit a frequency splitting of $\Delta_B/2\pi = 6.322$ kHz at the avoided crossing voltage $U_{B,a} = U_{B,i} + 1.958$ V = 12.358 V and the conversion factor is determined as $\zeta_B = 19.224$ kHz/V. Figure 4 a depicts a color-coded two-dimensional map of the normalized squared return amplitude in dependence of the inverse voltage sweep rate $1/\beta$ and the peak voltage U_p . The gray dotted line indicates the avoided crossing voltage $U_{B,a}$. We observe clear interference fringes in the normalized squared return amplitude even for peak voltages near or smaller than the avoided crossing voltage ($\tilde{U}_p \lesssim U_{B,a}$). This fact proves that the two modes interfere without the explicit need of traversing the avoided crossing and clearly indicates the importance of finite time dynamics in Stückelberg interferometry.

Calculating the theoretical return probability using the exact solution via finite time dynamics from Eq. (17) with no free parameters yields good agreement between experiment and theory as displayed in Fig. 4 b. Because of the longer duration ramps applied to sample B (up to $\vartheta = 1.0$ ms), the mechanical damping needs to be taken into account. Modelling the mechanical damping by an exponential decay with average energy decay time⁹ $t_0 = 5.7$ ms, the evolution of the modes after the double sweep through the avoided crossing is given by

$$|c_j(t)|^2 = \exp[-t/t_0] P_{1 \rightarrow j}, \quad (28)$$

with $P_{1 \rightarrow j}$ the return probability to mode $j = 1$ or $j = 2$. Note that Eq. (28) is applied to all three different theoretical approaches in the following.

In Fig. 4 b, the self-interference of the two-mode system clearly extends beyond the dotted line which represents the position of the avoided crossing at voltage $U_{B,a}$. Additionally, the theory exhibits distinct features in the interference pattern which are not reproduced by the experiment. In order to experimentally resolve these features, the system needs to interfere precisely with the same constant parameters in every particular measurement pixel from Fig. 4 a. Since the experiments are performed at room temperature, the system parameters vary strongly from measurement to measurement due to temperature fluctuations. Experimentally, we partially account for this effect by the implementation of an initialization voltage feedback loop⁹, which ensures the initialization of the system at the same resonance frequency, at least within one horizontal line from Fig. 4 a. Nevertheless, the fluctuations and uncertainties prevent the system from interfering with the precise same parameters in every particular measurement. Further information on the experimental uncertainties is provided elsewhere⁹. Note that the experimental data in Fig. 4 a is taken in a non-consecutive way

over a timespan of approximately 6 months which clearly demonstrates the validity of the data.

The results for the asymptotic theory (appendix A) are depicted in Fig. 4 c. The asymptotic theory reproduces the exact finite time solution with excellent agreement over the full displayed parameter range. Consequently, one can exploit the piecewise definition of the asymptotic theory in appendix A to deduce the characteristic dynamics of the system in each particular parameter regime. A detailed discussion of the different regimes will be given in chapter IV C.

Figure 4 d depicts the return probability calculated from the adiabatic impulse model [Eq. (26)] using the same parameters as for the exact solution via finite times. The model is depicted for the complete experimentally investigated parameter regime. However, certain displayed parameter ranges flaw the basic assumptions of the adiabatic impulse model that the dynamics of the system is fully adiabatic and governed by “infinite times” as described in chapter III D. Since there is no sharp transition for the validity of the model, the full parameter range is displayed. Additionally, the region below the avoided crossing voltage (gray dotted line) in Fig. 4 d is grayed out manually. The reason is that Eq. (26) is unphysical for the region where $\tilde{U}_p < U_{B,a}$ since the definition of the adiabatic impulse model requires traversing the avoided crossing.

In general, we observe a clear deviation between the adiabatic impulse model and both, the experimental data and the exact solution. In particular, the interference fringes of Fig. 4 d vanish for peak voltages in the region of the avoided crossing, when the dimensionless time of the phase evolution τ_p becomes comparable to the dimensionless level splitting η . This discrepancy clearly demonstrates that the dynamics of the system cannot be generally described by an infinite time approach where the two-mode interference is solely governed by the coupling of the system. However, for peak voltages, i.e., turning points far away from the avoided crossing, the result of the adiabatic impulse model qualitatively resembles the result obtained by the exact solution.

B. Interference visibility

In order to study the crossover from the infinite time limit to the finite time domain in more detail, we extract the interference visibility in dependence of the peak voltage from the

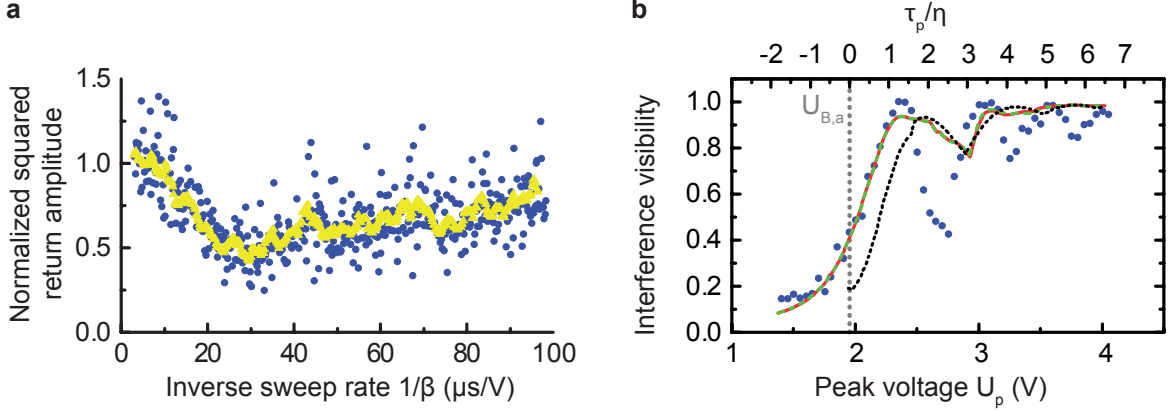


Figure 5. Interference visibility. **a**, Exemplary line-cut taken along the gray dotted line in Fig. 4a for illustration of the averaging of the experimental data. Blue dots represent the experimentally determined normalized squared amplitude versus inverse sweep rate $1/\beta$ for peak voltage $\tilde{U}_p \approx U_{B,a}$. Yellow triangles correspond to the averaged data using a moving average of 10 points. **b**, Interference visibility as a function of peak voltage U_p (bottom axis) and characteristic dimensionless ratio τ_p/η (top axis) extracted from horizontal line-cuts of Fig. 4b-d for the exact theoretical solution (red solid line), asymptotic theory (green dashed line) and adiabatic impulse model (black dotted line). Blue dots depict the interference visibility calculated from the *averaged* experimental data (yellow triangles in panel **a**) as described in the text.

experimental data and the different theoretical approaches. Note that by interference visibility we refer to the original definition of interference contrast³⁵ and not to the single-shot read-out-visibility as frequently referred to in e.g. spin systems³⁶. The interference visibility from the experimental data for a given peak voltage is calculated from the corresponding horizontal line-cut in Fig. 4a by the difference of the maximum and minimum normalized squared return amplitude divided by their sum³⁵. As exemplarily illustrated in Fig. 5a, we used a moving average of 10 points (see appendix D) in each respective horizontal line to account for experimental scatter of the data in the calculation of the interference visibility. The dataset corresponds to the line-cut along the gray dotted line in Fig. 4a where $\tilde{U}_p \approx U_{B,a}$. Figure 5b depicts the interference visibility as a function of peak voltage for the experimental data (blue dots) and the different theoretical models. Since the theoretical models represent real probabilities, we associate the interference visibility with the interference contrast, which is the difference of the maximum and the minimum return probability

without a normalization to their sum. The exact solution via finite times [red solid line, Eq. (17)] clearly exhibits a non-zero interference visibility for a set of peak voltages smaller than the avoided crossing voltage $U_{B,a}$ (gray dotted vertical line) in good agreement with the experimental data. The interference visibility obtained from the return probability in the asymptotic theory (green dashed line) nearly coincides with the result of the exact finite time solution. The underlying agreement clearly demonstrates that the exact solution of the double passage Stückelberg problem via finite times can be well-approximated by taking the asymptotic limit of the parabolic cylinder functions in the appropriate parameter regime. Furthermore, the analysis confirms the appearance of interference for peak voltages before the avoided crossing. In contrast, the adiabatic impulse model [black dotted line, Eq. (26)] interference visibility drops down close to zero for peak voltages smaller than $U_p \approx 2.0$ V, such that $\tilde{U}_p \approx U_{B,a}$.

To obtain a more intuitive understanding of the interference visibility, we replace the parameter U_p by introducing the ratio between two characteristic dimensionless scales, which are the dimensionless time τ_p and the dimensionless coupling η (see top x-axis in Fig. 5 b). As explained above [Eqs. (27)], τ_p corresponds to the distance from the avoided crossing to the turning point of the double sweep and hence becomes negative for sweeps where the avoided crossing is not passed (cf. top axis in Fig. 5 b). The dimensionless coupling η represents the effective level splitting between the two modes and is itself independent of the turning point in the double sweep [cf. Eqs. (27)]. Consequently, a characteristic dimensionless ratio of $\tau_p/\eta = 1$ would correspond to a population transfer from the lower to the upper mode with fidelity of 100 % using the generic picture of the Bloch sphere^{37,38} in the classical two-mode system¹⁹. Loosely speaking, the system has enough "time" to perform a complete population transfer to the upper mechanical mode when initialized in the lower mode. In principle, this characteristic behaviour can be extracted from the interference visibility depicted in Fig. 5 b. For $\tau_p/\eta = 1$ the interference visibility of the experimental data (blue dots) and the exact theoretical finite time solution (red solid line) reaches a maximum which is close to unity. At this point, we recover the full interference contrast since the two modes have the ability to interfere fully destructive due to the possibility of a complete population transfer. However, the interference visibility extracted from the theory saturates to a value of approximately 94 % whereas the experimental data converges to 100 % visibility. The origin of this discrepancy in the theory is attributed to the fact

that the interference pattern in Fig. 4 b is calculated for the parameter range in which the experiment is conducted. The fastest voltage sweeps are performed at an inverse sweep rate of $1/\beta = 3 \mu\text{s}/\text{V}$. Whereas experimental scatter of the data allows for a visibility of 100 %, the theory does not incorporate sufficiently fast sweeps to return to the same mode with a probability of unity, i.e., the sweeps are not non-adiabatic enough. In the limit $1/\beta \rightarrow 0$, the theory would simultaneously exhibit a 100 % visibility at $\tau_p/\eta = 1$. For $\tau_p/\eta \gg 1$ the theory curve also converges to 100 % visibility since the horizontal line-cuts from Fig. 4 intersect at least one constructive and one destructive interference fringe. Furthermore, we observe a reduced interference visibility in certain regions, where the return probability does not completely drop down to zero. We attribute this to the hyperbolic shape of the observed interference fringes in the displayed parameter space representation of the return probability as a function of inverse sweep rate and peak voltage. One could easily find horizontal line-cuts in Fig. 4 where the return probability does not completely drop down to zero, which translates into a reduced interference visibility. In this work, it is not investigated further if there is a distinct physical origin of this reduction in interference visibility.

In contrast to the above findings, the interference visibility extracted from the adiabatic impulse model (black dotted line) peaks for a larger ratio of $\tau_p/\eta \approx 1.5$, which clearly demonstrates that this model is only valid if the turning point is far away from the avoided crossing. However, we recover qualitatively similar dips in the interference visibility as in the exact finite time solution and the experimental data.

For larger ratios of τ_p/η , i.e. $\eta/\tau_p \ll 1$, the interference visibility extracted from the adiabatic impulse model coincides with the exact finite time solution. This result is in excellent agreement with the definition of the adiabatic impulse model as the infinite time limit of the finite time Stückelberg theory [cf. section III C 2].

C. Parameter regimes

In this section, we exploit the piecewise definition of the asymptotic limit of the exact theoretical finite time solution given in appendices A & B to quantify specific parameter regimes of Stückelberg interferometry. Depending on the specific regime, the characteristic times [Eqs. (27)] are limited to certain boundaries. These boundaries, in turn, allow for the quantification of the underlying physics governing the coupled system dynamics.

In order to asymptotically expand the parabolic cylinder functions, we define a critical dimensionless time τ_{crit} . This critical dimensionless time serves as a measure for the employed dimensionless times τ_i , τ_p and τ_f in the theory. Those parameters can either be bound by τ_{crit} ($-\tau_{\text{crit}} \leq \tau \leq \tau_{\text{crit}}$) or unbound ($|\tau| > \tau_{\text{crit}}$). Here, one should keep in mind that τ_i is defined as smaller than zero. As further discussed in appendix A, the parabolic cylinder functions can mathematically be approximated by a power series. Hereby, the magnitude of τ_{crit} specifies up to which order the power series is expanded. For the following calculations we defined $\tau_{\text{crit}} = 2$.

Figure 6 depicts the theoretical return probability calculated from the asymptotic theory as in Fig. 4 c for an extended peak voltage range. The layover in Fig. 6 displays the boundary lines of the different parameter regimes from which the asymptotic solution is calculated. We recover six different parameter regimes, labeled by roman numerals from I to VI, which are specified in Table I. As can be seen immediately from Table I, there is only one regime where

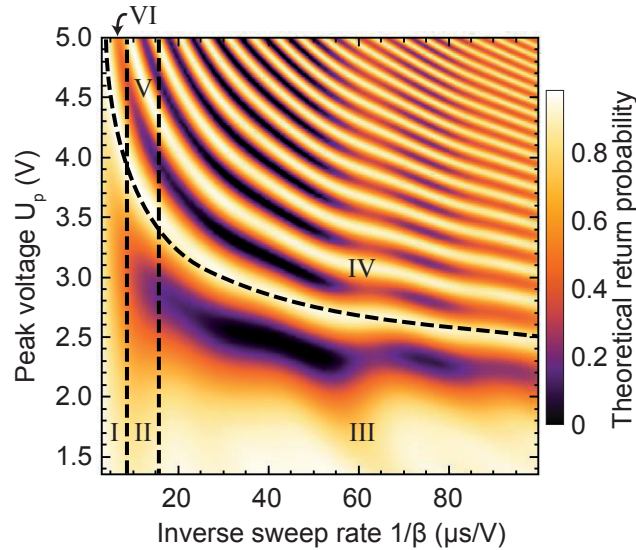


Figure 6. Phase space of the parameter regimes in the asymptotic theory. Color-coded theoretical return probability as calculated from the asymptotic theory (cf. Fig. 4 c) for an extended peak voltage range. Black dashed lines indicate the border-lines of the different parameter regimes in the asymptotic theory. The different parameter regimes are labeled by roman numerals which are elucidated in Table I.

all three characteristic times are above threshold, which is regime IV. Since the characteristic times are not bound in this regime it is considered as the long time limit, which includes the

Regime	τ_i	τ_p	τ_f
I	$-\tau_{\text{crit}} \leq \tau_i \leq \tau_{\text{crit}}$	$-\tau_{\text{crit}} \leq \tau_p \leq \tau_{\text{crit}}$	$-\tau_{\text{crit}} \leq \tau_f \leq \tau_{\text{crit}}$
II	$\tau_i < -\tau_{\text{crit}}$	$-\tau_{\text{crit}} \leq \tau_p \leq \tau_{\text{crit}}$	$-\tau_{\text{crit}} \leq \tau_f \leq \tau_{\text{crit}}$
III	$\tau_i < -\tau_{\text{crit}}$	$-\tau_{\text{crit}} \leq \tau_p \leq \tau_{\text{crit}}$	$\tau_f > \tau_{\text{crit}}$
IV	$\tau_i < -\tau_{\text{crit}}$	$\tau_p > \tau_{\text{crit}}$	$\tau_f > \tau_{\text{crit}}$
V	$\tau_i < -\tau_{\text{crit}}$	$\tau_p > \tau_{\text{crit}}$	$-\tau_{\text{crit}} \leq \tau_f \leq \tau_{\text{crit}}$
VI	$-\tau_{\text{crit}} \leq \tau_i \leq \tau_{\text{crit}}$	$\tau_p > \tau_{\text{crit}}$	$\tau_f > \tau_{\text{crit}}$

Table I. Summary of the different asymptotic regimes.

infinite time limit, e.g. the adiabatic impulse model, where $\eta/\tau_f, \eta/|\tau_i|, \eta/\tau_p \ll 1$. However, there is no sharp border between the long time limit and the infinite time limit. Whereas the former requires the dimensionless times to be much larger than one, the latter exhibits the additional constraint that the dimensionless times are large compared to the dimensionless coupling. In this infinite time limit, the dynamics of the strongly coupled two-mode system is governed by the coupling strength of the two modes since the exact evolution in terms of dimensionless time plays a minor role. In fact, this is the only regime which, to the best of our knowledge, has been considered in the past in the framework of Landau-Zener type physics^{16,31,32} and Stückelberg interferometry¹⁶, except for the work of *Vitanov et al.*²⁹ and Refs. 12 and 39. Nevertheless and as one can easily deduce from Fig. 6, a complete solution of the double passage Stückelberg problem is in crucial need of additional parameter regimes, where the finite durations of the sweeps play a major role.

The transition from the long time limit to the finite time domain is represented by the hyperbolic black dashed line in Fig. 6. Associating a threshold peak voltage $U_{\text{p,crit}}$ with this transition, one can easily calculate the border-line as a function of inverse sweep rate via the definitions of τ_p [cf. Eqs. (27)] and $\tau_{\text{crit}} = 2$

$$\begin{aligned}
U_{\text{p,crit}} &= \sqrt{\frac{2}{\pi\zeta}} \frac{1}{\sqrt{1/\beta}} + (U_{\text{B,a}} - U_{\text{B,i}}) \\
&\approx \sqrt{\frac{2}{\pi\zeta}} \frac{1}{\sqrt{1/\beta}} + 1.958 \text{ V}.
\end{aligned} \tag{29}$$

Accordingly, the two vertical border-lines in Fig. 6, which are independent of the peak voltage ($[1/\beta]_{\text{I}} = 8.64 \mu\text{s/V}$, $[1/\beta]_{\text{II}} = 15.58 \mu\text{s/V}$), can be calculated straight forward from Eqs. (27). Note that for $\tau_i = -\tau_f$, i.e., if the system could be read-out at the initialization point after a

symmetric voltage ramp, the right vertical border-line in Fig. 6 would vanish. Even though regime II and regime V are exclusively observed in our particular measurement scheme, the importance of finite time effects in Stückelberg interferometry is definitely pointed out by the presence of regimes I, III and VI. Especially regime I and III are of great interest since they reveal the dynamics of Stückelberg interferometry between two strongly coupled modes without the explicit need of traversing the avoided energy level crossing.

Since the dynamics of the strongly coupled classical two-mode system can be mapped onto the dynamics of a quantum mechanical two-level system in Stückelberg interferometry⁹, the same regimes are existent in every quantum mechanical two-level system such as e.g. superconducting qubits^{13–15,17} or spin-1/2 systems^{10–12}. To the best of our knowledge, such regimes have so far not been investigated in the framework of Stückelberg interferometry and might be a prominent candidate for future investigations of quantum two-level systems.

V. CONCLUSION

In conclusion, we have demonstrated the importance of finite time effects in Stückelberg interferometry. Providing a complete and exact theoretical solution to the double passage Stückelberg problem, we have shown that the commonly employed adiabatic impulse model¹⁶ does not address the full complexity of the problem¹⁸. In particular, the adiabatic impulse model solely describes one single parameter regime, where the dynamics of the system is completely governed by the coupling of the two modes corresponding to an infinite time limit. We have been able to asymptotically expand the provided exact finite time theoretical model and have hereby classified previously undiscovered parameter regimes in Stückelberg interferometry. The theoretical findings have been confirmed in remarkably good agreement by a detailed experimental study of the dynamics of a classical two mode system^{19,26} realized by two strongly coupled high quality factor nanomechanical string resonator modes. All theoretically predicted parameter regimes have been demonstrated experimentally by a thorough investigation of classical Stückelberg interferometry⁹. We observed clear oscillations in the experimentally accessible normalized squared return amplitude, even without traversing the avoided crossing in excellent agreement with the provided exact theory. These findings have been supported by a detailed study of the interference visibility over a huge parameter range. Interestingly, the dynamics of the investigated classical two-mode system can be mapped to

the dynamics of quantum mechanical two-level systems, as has recently been demonstrated by the authors⁹. As a consequence, the above theoretical findings can be applied one-to-one to quantum mechanical two-level systems.

Appendix A: Asymptotic expansion of the parabolic cylinder function

In this section we list the asymptotic expansions used to produce Fig. 4c and Fig. 6.

1. Short-time expansion

When $-\tau_{\text{crit}} < \tau < \tau_{\text{crit}}$, one can approximate parabolic cylinder functions by a power series. In this work we used one of the power series derived in Ref. 40,

$$D_{\nu}(\tau) = \sqrt{\pi} 2^{\frac{\nu}{2}} \exp\left(\frac{\tau^2}{4}\right) \sum_{n=0}^{\infty} \frac{(-\sqrt{2}\tau)^n}{n! \Gamma\left[\frac{1}{2}(1 - \nu - n)\right]}. \quad (\text{A1})$$

This expansion is particularly useful when $|\tau_{\text{crit}}| \ll 1$ since the series can be truncated after a few terms.

Here, we are going to choose $|\tau_{\text{crit}}| = 2$. While we will not be able to truncate the series to only one or two terms, we will be able to approximate the parabolic cylinder functions with only two different functions. The special values $|\tau_{\text{crit}}| = 2$ correspond then to the point where the functions are matched.

2. Long-time expansion

When $\tau \gg 1$, one can use the results of Ref. 41 to find asymptotic expansions for the relevant parabolic cylinder functions involved in Eqs. (13) and (14). The asymptotic

expansions are

$$\begin{aligned}
D_{-i\frac{\eta^2}{4}-1} \left(e^{i\frac{\pi}{4}} \tau \right) &\simeq \frac{2}{\eta} \sin[\theta(\tau)] \exp \left[\frac{\pi\eta^2}{16} - i \left(\xi(\tau) + \frac{\pi}{4} \right) \right], \\
D_{-i\frac{\eta^2}{4}-1} \left(e^{-i\frac{3\pi}{4}} \tau \right) &\simeq \frac{2}{\eta} \sin[\theta(\tau)] \exp \left[-3\frac{\pi\eta^2}{16} - i \left(\xi(\tau) - \frac{3\pi}{4} \right) \right] \\
&\quad + \frac{\sqrt{2\pi}}{\Gamma \left(1 + i\frac{\eta^2}{4} \right)} \cos[\theta(\tau)] \exp \left[-\frac{\pi\eta^2}{16} + i\xi(\tau) \right], \\
D_{-i\frac{\eta^2}{4}} \left(e^{-i\frac{3\pi}{4}} \tau \right) &\simeq \cos[\theta(\tau)] \exp \left[-3\frac{\pi\eta^2}{16} - i\xi(\tau) \right] \\
&\quad + \frac{\eta\sqrt{\pi}}{\sqrt{2}\Gamma \left(1 + i\frac{\eta^2}{4} \right)} \sin[\theta(\tau)] \exp \left[\frac{-\pi\eta^2}{16} + i \left(\xi(\tau) + \frac{\pi}{4} \right) \right], \\
D_{-i\frac{\eta^2}{4}} \left(e^{i\frac{\pi}{4}} \tau \right) &\simeq \cos[\theta(\tau)] \exp \left[\frac{\pi\eta^2}{16} - i\xi(\tau) \right],
\end{aligned} \tag{A2}$$

where we have defined

$$\begin{aligned}
\sin[\theta(\tau)] &= \sqrt{\frac{1}{2} \left(1 - \frac{\tau}{\sqrt{\tau^2 + \eta^2}} \right)}, \\
\cos[\theta(\tau)] &= \sqrt{\frac{1}{2} \left(1 + \frac{\tau}{\sqrt{\tau^2 + \eta^2}} \right)}, \\
\xi(\tau) &= -\frac{\eta^2}{8} + \frac{\eta^2}{4} \log \left[\frac{1}{2} \left(\tau + \sqrt{\tau^2 + \eta^2} \right) \right] + \frac{\tau}{4} \sqrt{\tau^2 + \eta^2}.
\end{aligned} \tag{A3}$$

Note that this expansion is employed for $\tau \geq \tau_{\text{crit}}$.

Finally, we would like to draw attention to the fact that Eq. (A2) is also valid for the weaker condition $\tau^2 + \eta^2/4 \gg 1$.

a. “Negative” long-time expansion

To obtain the asymptotic expansions for negative arguments, $\tau < 0$ and $|\tau| \gg 1$, one substitutes $\tau \rightarrow e^{\pm i\pi} |\tau|$ in the argument of the functions to be expanded. With this substitution, the problem is reduced to the cases presented in Eqs. (A2).

b. Expansion of $[D_\nu(z)]^$*

Since the parabolic functions are analytic, we have $[D_\nu(z)]^* = D_{\nu^*}(z^*)$. As a consequence, the asymptotic expansion of $D_{\nu^*}(z^*)$ is the complex conjugate of the asymptotic expansion

of $D_\nu(z)$.

Appendix B: Leading order correction to the return probability in the infinite-time limit

As explained in the main text, we have defined the infinite-time limit as $\eta/\tau, \eta/|\tau_i|, \eta/\tau_p \ll 1$. To obtain the first-order correction to Eq. (20), we use Eqs. (18) and (19) and expand $\cos[\theta(\tau)]$ and $\sin[\theta(\tau)]$ in powers of η/τ . In contrast to what has been presented in the main text, we keep the lowest contribution in η/τ . We find

$$\cos[\theta(\tau)] = 1 - \frac{1}{8} \frac{\eta^2}{\tau^2} + \mathcal{O}\left(\frac{\eta^3}{\tau^3}\right), \quad (\text{B1})$$

and

$$\sin[\theta(\tau)] = \frac{1}{2} \frac{\eta}{\tau} + \mathcal{O}\left(\frac{\eta^3}{\tau^3}\right). \quad (\text{B2})$$

We find that the leading order correction is given by

$$\begin{aligned} P_{1 \rightarrow 1}^{(1)} = & \frac{\eta}{\sqrt{2}} \sqrt{P_{\text{LZ}}} \sqrt{1 - P_{\text{LZ}}} \times \\ & \left\{ -2 \frac{\cos[\xi(\tau) - \xi(\tau_i)]}{\tau_p} [P_{\text{LZ}}(\sin[\chi_1(\tau, \tau_i)] - \cos[\chi_1(\tau, \tau_i)]) \right. \\ & \quad + (1 - P_{\text{LZ}})(\cos[\chi_2(\tau, \tau_p, \tau_i)] + \sin[\chi_2(\tau, \tau_p, \tau_i)])] \\ & + 2 \frac{\cos[\xi(\tau) - \xi(\tau_p)]}{\tau} [P_{\text{LZ}}(\sin[\chi_3(\tau, \tau_p)] + \cos[\chi_3(\tau, \tau_p)]) \\ & \quad + (1 - P_{\text{LZ}})(\cos[\chi_4(\tau, \tau_p)] - \sin[\chi_4(\tau, \tau_p)])] \\ & - 2 \frac{\sin[\xi(\tau_i) - \xi(\tau_p)]}{\tau_i} [P_{\text{LZ}} 2 \cos[\xi(\tau_i) - \xi(\tau_p)](\cos[\chi_5(\tau_p)] + \sin[\chi_5(\tau_p)]) \\ & \quad \left. - (\cos[\chi_6(\tau_i, \tau_p)] + \sin[\chi_6(\tau_i, \tau_p)])] \right\}, \end{aligned} \quad (\text{B3})$$

where we have defined

$$\begin{aligned}
\chi_1(\tau, \tau_i) &= \xi(\tau) + \xi(\tau_i) - \arg \left[\Gamma \left(1 + i \frac{\eta^2}{4} \right) \right], \\
\chi_2(\tau, \tau_p, \tau_i) &= \xi(\tau) + \xi(\tau_i) + 4\xi(\tau_p) - 3\arg \left[\Gamma \left(1 + i \frac{\eta^2}{4} \right) \right], \\
\chi_3(\tau, \tau_p) &= \xi(\tau) - 3\xi(\tau_p) + \arg \left[\Gamma \left(1 + i \frac{\eta^2}{4} \right) \right], \\
\chi_4(\tau, \tau_p) &= \xi(\tau) + \xi(\tau_p) - \arg \left[\Gamma \left(1 + i \frac{\eta^2}{4} \right) \right], \\
\chi_5(\tau_p) &= 2\xi(\tau_p) - \arg \left[\Gamma \left(1 + i \frac{\eta^2}{4} \right) \right], \\
\chi_6(\tau_i, \tau_p) &= \xi(\tau_i) + \xi(\tau_p) - \arg \left[\Gamma \left(1 + i \frac{\eta^2}{4} \right) \right],
\end{aligned} \tag{B4}$$

and $\xi(\tau)$ is defined in Eq. (A3).

If we define (see Eq. (20) in the main text)

$$P_{1 \rightarrow 1}^{(0)} = 1 - 4P_{\text{LZ}}(1 - P_{\text{LZ}}) \cos^2[\chi_{\text{dp}}(\tau_p)] = P_{1 \rightarrow 1}^{\text{inf}}, \tag{B5}$$

then the return probability to leading order in $\eta/\tau, \eta/\tau_i, \eta/\tau_p$ is given by

$$P_{1 \rightarrow 1} = P_{1 \rightarrow 1}^{(0)} + P_{1 \rightarrow 1}^{(1)} + \mathcal{O} \left(\frac{\eta^2}{\tau^2}, \frac{\eta^2}{\tau_p^2}, \frac{\eta^2}{\tau_i^2} \right) \tag{B6}$$

Appendix C: Voltage ramps

The experimentally applied triangular voltage ramps are created numerically and fed to an Arbitrary Function Generator (AFG). A schematic of the applied ramps is depicted in Fig. C.1. The ramps consist of a total of 500,000 samples (500 kSa) divided into four basic regions. The first region is a $t_{\text{trigger}} = 5 \text{ ms}$ long window in which a trigger command is sent from the AFG to the spectrum analyzer to start the measurement, during which the additional ramp voltage is kept at zero and hence the absolute voltage is at base level U_i of the initialization voltage. The triangular voltage ramp itself (region two) consists in total of 1,000 samples (1 kSa), with 500 Sa per ramp flank. The sweep voltage is ramped up from zero to the peak voltage U_p with sample rate

$$\text{Samplerate} = \frac{500 \text{ Sa}}{U_p \times 1/\beta}, \tag{C1}$$

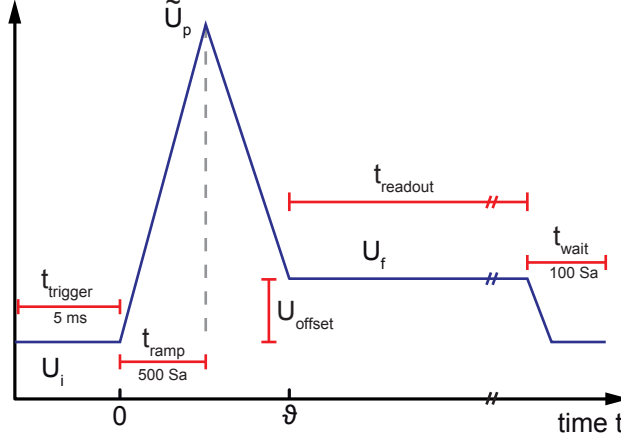


Figure C.1. Illustration of the applied voltage ramps. The time axis is truncated as a guide to the eye since the read-out time t_{readout} is much longer than the ramp time t_{ramp} .

from which we deduce the inverse sweep rate $1/\beta$. The corresponding ramp time is hence given by

$$t_{\text{ramp}} = \frac{500 \text{ Sa}}{\text{Samplerate}} = U_p \times 1/\beta. \quad (\text{C2})$$

The right hand side flank of the triangular voltage ramp decreases the absolute voltage from \tilde{U}_p to the read-out voltage U_f , which is off-set from the initialization voltage U_i by $U_{\text{offset}} = 0.5 \text{ V}$. As described in the main text, the exponential decay of the returning excitation has to be measured at a different read-out frequency since the resonant sinusoidal drive tone at fixed frequency $\omega_1(U_i)/2\pi$ cannot be turned off during the voltage ramp. Hence, the above introduced voltage off-set is employed. It is important to note that the voltage off-set has to be adjusted in such a way, that the mechanical resonance at the read-out voltage $\omega_1(U_f)/2\pi$ is not excited by the resonant drive tone at $\omega_1(U_i)/2\pi$. The exponential decay of the mechanical resonance after the triangular voltage ramp is measured in region three using a spectrum analyzer in a timespan of

$$\begin{aligned} t_{\text{readout}} &= t_{\text{ramp}} \times \frac{\text{Total Samples}}{500 \text{ Sa}} - 2 \times t_{\text{ramp}} \\ &= U_p \times 1/\beta \left(\frac{500 \text{ kSa}}{500 \text{ Sa}} - 2 \right). \end{aligned} \quad (\text{C3})$$

After the measurement, the absolute voltage is ramped back from U_f to the initialization voltage U_i (region four) by decreasing the sweep voltage from U_{offset} to zero, which takes 100 samples of the total sample number of 500 kSa.

Appendix D: Moving average

A moving average, also referred to as sliding average, is a statistical tool for the smoothing of datasets. Consider a dataset of N elements. Then, a moving average of M points creates $N - M$ subsets of elements, which are averaged individually. For each element $n \geq M$ of dataset N , the moving average yields the mean of the subset which consists of element n and the preceding $M - 1$ elements in the dataset:

$$\bar{p}_n = \frac{1}{M} \sum_{i=0}^{M-1} p_{n-i} \quad (\text{D1})$$

A moving average over 10 points is applied to the experimental data to extract the measurement visibility. The effect of a moving average of 10 points on the experimental data is exemplarily depicted in Fig. 5 a.

ACKNOWLEDGMENTS

Financial support by the Deutsche Forschungsgemeinschaft via the collaborative research center SFB 767 and via project Ko 416-18 is gratefully acknowledged. H. R. acknowledges funding from the Swiss SNF.

* maximilian.seitner@uni-konstanz.de

- ¹ R. Riedinger, S. Hong, R. A. Norte, J. A. Slater, J. Shang, A. G. Krause, V. Anant, M. Aspelmeyer, and S. Gröblacher, *Nature* **530**, 313 (2016).
- ² V. Sudhir, D. J. Wilson, R. Schilling, H. Schütz, A. Ghadimi, A. Nunnenkamp, and T. J. Kippenberg, *ArXiv e-prints* (2016), arXiv:1602.05942 [quant-ph].
- ³ N. Spethmann, J. Kohler, S. Schreppler, L. Buchmann, and D. M. Stamper-Kurn, *Nature Physics* **12**, 27 (2016).
- ⁴ E. E. Wollman, C. U. Lei, A. J. Weinstein, J. Suh, A. Kronwald, F. Marquardt, A. A. Clerk, and K. C. Schwab, *Science* **349**, 952 (2015).
- ⁵ H. Xu, D. Mason, L. Jiang, and J. G. E. Harris, *Nature* **537**, 80 (2016).
- ⁶ N. Rossi, F. R. Braakman, D. Cadeddu, D. Vasyukov, G. Tütüncüoğlu, A. F. i. Morral, and M. Poggio, *ArXiv e-prints* (2016), arXiv:1604.01073 [cond-mat.mes-hall].

- ⁷ L. Mercier de Lépinay, B. Pigeau, B. Besga, P. Vincent, P. Poncharal, and O. Arcizet, ArXiv e-prints (2016), arXiv:1604.01873 [cond-mat.mes-hall].
- ⁸ H. Okamoto, R. Schilling, H. Schütz, V. Sudhir, D. J. Wilson, H. Yamaguchi, and T. J. Kippenberg, Applied Physics Letters **108**, 153105 (2016).
- ⁹ M. J. Seitner, H. Ribeiro, J. Kölbl, T. Faust, J. P. Kotthaus, and E. M. Weig, ArXiv e-prints (2016), arXiv:1602.01034 [cond-mat.mes-hall].
- ¹⁰ J. R. Petta, H. Lu, and A. C. Gossard, Science **327**, 669 (2010).
- ¹¹ L. Gaudreau, G. Granger, A. Kam, G. C. Aers, S. A. Studenikin, P. Zawadzki, M. Pioro-Ladriere, Z. R. Wasilewski, and A. S. Sachrajda, Nature Physics **8**, 54 (2012).
- ¹² H. Ribeiro, G. Burkard, J. R. Petta, H. Lu, and A. C. Gossard, Physical Review Letters **110**, 086804 (2013).
- ¹³ W. D. Oliver, Y. Yu, J. C. Lee, K. K. Berggren, L. S. Levitov, and T. P. Orlando, Science **310**, 1653 (2005).
- ¹⁴ M. Sillanpää, T. Lehtinen, A. Paila, Y. Makhlin, and P. Hakonen, Physical Review Letters **96**, 187002 (2006).
- ¹⁵ M. D. Lahaye, J. Suh, P. M. Echternach, K. C. Schwab, and M. L. Roukes, Nature **459**, 960 (2009).
- ¹⁶ S. N. Shevchenko, S. Ashhab, and F. Nori, Physics Reports **492**, 1 (2010).
- ¹⁷ S. N. Shevchenko, S. Ashhab, and F. Nori, Physical Review B **85**, 094502 (2012).
- ¹⁸ E. C. G. Stückelberg, Helvetica Physica Acta **5**, 369 (1932).
- ¹⁹ T. Faust, J. Rieger, M. J. Seitner, J. P. Kotthaus, and E. M. Weig, Nature Physics **9**, 485 (2013).
- ²⁰ T. Faust, P. Krenn, S. Manus, J. P. Kotthaus, and E. M. Weig, Nature Communications **3**, 728 (2012).
- ²¹ J. Rieger, T. Faust, M. J. Seitner, J. P. Kotthaus, and E. M. Weig, Applied Physics Letters **101**, 103110 (2012).
- ²² Q. P. Unterreithmeier, E. M. Weig, and J. P. Kotthaus, Nature **458**, 1001 (2009).
- ²³ T. Faust, J. Rieger, M. J. Seitner, P. Krenn, J. P. Kotthaus, and E. M. Weig, Physical Review Letters **109**, 037205 (2012).
- ²⁴ G. Sun, X. Wen, B. Mao, Y. Yu, J. Chen, W. Xu, L. Kang, P. Wu, and S. Han, Physical Review B **83**, 180507 (2011).

- ²⁵ L. Novotny, American Journal of Physics **78**, 1199 (2010).
- ²⁶ H. Okamoto, A. Gourgout, C.-Y. Chang, K. Onomitsu, I. Mahboob, E. Y. Chang, and H. Yamaguchi, Nature Physics **9**, 480 (2013).
- ²⁷ A. B. Shkarin, N. E. Flowers-Jacobs, S. W. Hoch, A. D. Kashkanova, C. Deutsch, J. Reichel, and J. G. E. Harris, Physical Review Letters **112**, 013602 (2014).
- ²⁸ B. W. Shore, M. V. Gromovyy, L. P. Yatsenko, and V. I. Romanenko, American Journal of Physics **77**, 1183 (2009).
- ²⁹ N. V. Vitanov and B. M. Garraway, Physical Review A **53**, 4288 (1996).
- ³⁰ V. I. Arnold, A. Weinstein, and K. Vogtman-Arnold, *Mathematical Methods Of Classical Mechanics*, 2nd ed. (Springer-Verlag, 1989).
- ³¹ L. D. Landau, Physics of the Soviet Union **2**, 46 (1932).
- ³² C. Zener, Proceedings of the Royal Society of London Series A **137**, 696 (1932).
- ³³ E. Majorana, Nuovo Cimento **9**, 43 (1932).
- ³⁴ R. E. Meyer, SIAM Review **31**, 435 (1989).
- ³⁵ B. E. A. Saleh and M. C. Teich, *Fundamentals of Photonics*, second edition ed. (Wiley-Interscience, 2007) p. 420.
- ³⁶ A. Morello, J. J. Pla, F. A. Zwanenburg, K. W. Chan, K. Y. Tan, H. Huebl, M. Möttönen, C. D. Nugroho, C. Yang, J. A. van Donkelaar, A. D. C. Alves, D. N. Jamieson, C. C. Escott, L. C. L. Hollenberg, R. G. Clark, and A. S. Dzurak, Nature **467**, 687 (2010).
- ³⁷ M. A. Nielsen and I. L. Chuang, *Quantum Computation and Quantum Information* (Cambridge University Press, 2000).
- ³⁸ D. Dragoman and M. Dragoman, eds., *Quantum-Classical Analogies* (Springer, 2004) p. 120ff.
- ³⁹ H. Ribeiro, J. R. Petta, and G. Burkard, Physical Review B **87**, 235318 (2013).
- ⁴⁰ K. M. Abadir, Journal of Physics A: Mathematical and General **26**, 4059 (1993).
- ⁴¹ F. W. J. Olver, J. Res. Natl. Bur. Stand. **63B**, 131 (1959).